Collapse of ferromagnetism with Ti doping in $Sm_{0.55}Sr_{0.45}MnO_3$

Prosenjit Sarkar,[1,*] Nazir Khan,[2,†] Kalpataru Pradhan,[2,‡] and Prabhat Mandal[2,§]
[1]*Department of Physics, Serampore College, Serampore 712201, India*
[2]*Saha Institute of Nuclear Physics, HBNI, 1/AF Bidhannagar, Calcutta 700064, India*

(Received 6 April 2018; published 20 July 2018)

We have investigated the effect of Ti doping on the transport properties coupled with the magnetic ones in $Sm_{0.55}Sr_{0.45}Mn_{1-\eta}Ti_\eta O_3$ ($0 \leqslant \eta \leqslant 0.04$). The parent compound, $Sm_{0.55}Sr_{0.45}MnO_3$, exhibits a first-order paramagnetic-insulator to ferromagnetic-metal transition just below $T_c = 128$ K. With the substitution of Ti at Mn sites (B site), T_c decreases approximately linearly at the rate of 22 $K\%^{-1}$ while the width of thermal hysteresis in magnetization and resistivity increases almost in an exponential fashion. The most spectacular effect has been observed for the composition $\eta = 0.03$, where a magnetic field of only 1 T yields a huge magnetoresistance, $1.2\times10^7\%$ at $T_c \approx 63$ K. With increasing magnetic field, the transition shifts towards higher temperature side, and the first-order nature gets weakened and eventually becomes crossover above a critical field (H_{cr}) which increases with Ti doping. For $\eta \geqslant 0.04$, the system remains insulting without any ferromagnetic ordering down to 2 K. The Monte Carlo calculations based on a two-band double exchange model reveal that the rapid suppression of ferromagnetism with Ti doping is due to the increase of the lattice distortions around the doped Ti ions.

DOI: 10.1103/PhysRevB.98.014422

I. INTRODUCTION

Perovskite manganites of the form $R_{1-x}A_xMnO_3$ (R denotes rare-earth ions and A denotes alkaline-earth ions) display rich varieties of physical phenomena due to the complex interplay between spin, charge, and orbital degrees of freedom [1–6]. The competition between these degrees of freedom is most prominently manifested in narrowband system with disorder. Usually, two types of disorder are considered in manganites. One is A-site disorder, namely the quenched disorder, which arises mainly due to the size mismatch between R and A cations, and the other is B(Mn)-site disorder, which originates due to the partial substitution of Mn by other transition-metal ions with a different spin and valence state. Several studies have shown that the disorder at the A-site has a strong influence on different kinds of long-range ordering of a manganese sublattice. Among these ordered phases, the charge-ordered (CO) state is most sensitive to A-site disorder while the ferromagnetic (FM) -metallic phase is relatively weakly affected [7–21]. On the other hand, the doping at the B-site induces local disorder directly into the Mn-O-Mn network, and as a result it has a much stronger effect on magnetic, transport, and other physical properties of the system as compared to A-site disorder. Only a few percent of B-site doping can bring about a drastic change in the electronic and magnetic properties without a significant change in the crystal structure. Several experiments have been performed on a large number of combinations of reference states and B-site dopants [22–34]. On the basis of a reference state, two classes of materials can be distinguished: (i) FM metal at $x \approx 0.3$–0.4 and (ii) CO insulator at around $x \approx 0.5$ [35]. In half-doped CO manganites, often substitution of a small amount of Cr/Ni/Ru at the Mn site dramatically suppresses the long-range CO state and drives the system into a FM metallic state. On the contrary, the B-site doping in FM manganites may result in a strong suppression of ferromagnetism by localizing the charge carriers, which leads to the formation of an inhomogeneous and insulating magnetic ground state.

The effect of Mn-site doping on magnetic and transport properties has already been studied extensively but mostly on wide-band FM manganites [28–34]. However, the role of Mn-site doping in a narrowband FM system, in particular close to the multicritical point, has not been studied in great detail [28]. In mixed valance manganites, the effective bandwidth (W) of the e_g orbital of Mn $3d$ is one of the key parameters that determines the nature of the electronic and magnetic phases. The bandwidth of a system can be tuned by changing the average ionic radius (r_0) of R and A cations, $r_0 = (1-x)r_R + xr_A$ [1–6]. A decrease in r_0 leads to a decrease in the $\langle Mn-O-Mn\rangle$ bond angle (θ) from 180° degree, which in turn suppresses the effective d electron transfer interaction t between the neighboring Mn sites via oxygen $2p$ states, and as a result W decreases. As the $2p$ to $3d$ transfer interaction t_{pd} is proportional to $\cos\theta$, the effective d-d hopping interaction t or W is approximately proportional to t_{pd}^2 and hence to $\cos^2\theta$ [1–6]. For smaller rare-earth ions such as Sm, Eu, etc., the bandwidth becomes narrower and several interactions, such as charge/orbital ordering, antiferromagnetic interaction, and electron-phonon coupling, which compete with FM double-exchange, become comparable in strength and hence the effect of disorder on the physical properties is much stronger and spectacular in narrowband manganites [1–10]. For this reason, we focus on a narrowband manganite, $Sm_{0.55}Sr_{0.45}MnO_3$ (SSMO), which is located near

*psphysics1981@gmail.com
†nazirkhan91@gmail.com
‡kalpataru.pradhan@saha.ac.in
§prabhat.mandal@saha.ac.in

the multicritical point where the three phases, namely FM-metal, CO-insulator, and antiferromagnetic-insulator, compete strongly with each other to explore the role of Mn-site disorder on ferromagnetism [14–21]. The effect of B-site doping on magnetic and transport properties of $Sm_{0.55}Sr_{0.45}Mn_{1-\eta}Ti_{\eta}O_3$ with $0 \leqslant \eta \leqslant 0.04$ has been studied systematically. The results show that the FM-metal to paramagnetic (PM) -insulator transition in SSMO is first-order with transition temperature, $T_c \approx 128$ K. With the substitution of nonmagnetic Ti^{4+}, both the FM transition temperature, T_c, and the metal-insulator transition temperature (MIT), T_{MI}, decrease while the thermal hysteresis width (ΔT) in electrical resistivity (ρ) and magnetization (M) increases drastically. Only 3% Ti doping increases ΔT from 4.5 to 23.4 K. Such a huge increase in ΔT due to the small amount of substitution at the B-site has not been reported earlier in any FM manganite. The application of an external magnetic field (H) shifts the MIT toward higher temperature, leading to a field-dependent phase boundary. Besides these experimental findings, the role of B-site doping on transport and magnetic properties has been investigated using a model Hamiltonian. Our calculations based on the Monte Carlo technique using a two-band double exchange model including electron-phonon coupling, superexchange interactions, and quenched disorder reveal that with increasing Ti content, the lattice distortion around the Ti ions increases, and as a result T_c decreases, which qualitatively agrees with experimental results.

II. EXPERIMENTS

Polycrystalline $Sm_{0.55}Sr_{0.45}Mn_{1-\eta}Ti_{\eta}O_3$ samples with $\eta = 0$–0.04 were prepared by the conventional solid-state reaction technique. The starting materials, Sm_2O_3 (prefired), $SrCO_3$, Mn_3O_4, and TiO_2, were mixed in a stoichiometric ratio and ground thoroughly in an agate mortar by using ethanol. The mixture was put in a platinum crucible and calcined in air at 1100 °C for a few days with intermediate grindings. The obtained powder was pulverized and sintered at 1200 °C for 24 h to ensure the chemical homogeneity. Phase purity and the structural analysis of the samples were done by the powder x-ray diffraction (XRD) technique with Cu $K\alpha$ radiation in a high-resolution Rigaku x-ray diffractometer (TTRAX II). For all the studied compositions ($\eta = 0$–0.04), we did not observe any peak due to the impurity phase in the XRD pattern. The Rietveld refinement technique was used for the structural analysis. The dc magnetization measurements were performed using a superconducting quantum interference device-vibrating sample magnetometer (SQUID-VSM, Quantum Design). Resistivity measurements were performed by a conventional four-probe technique over a wide range of temperature for different applied magnetic fields up to 9 T. We have measured transport and magnetic properties as functions of H and T for all the samples, but for clarity only a few of them are presented.

III. RESULTS AND DISCUSSION

A. Crystal structure

Figure 1 shows the room-temperature powder x-ray diffraction of $Sm_{0.55}Sr_{0.45}Mn_{1-\eta}Ti_{\eta}O_3$ for four compositions, $\eta = 0$, 0.01, 0.02, and 0.03, as representatives. The diffraction patterns show that all the samples have a perovskite orthorhombic (space group $Pnma$) structure in which the atomic positions of Sm(Sr): $4c(x, 1/4, z)$, Mn(Ti): $4b(0, 0, 1/2)$, O1: $4c(x, 1/4, z)$, and O2: $8d(x, y, z)$ are used for indexing the Bragg peaks [36]. The crystal structure of the samples does not change with Ti doping. However, with increasing Ti concentration, the lattice parameters a, b, c and hence the unit-cell volume increase systematically, as shown in the inset of Fig. 1. The increase of the cell volume suggests the substitution of Mn^{4+} ions by Ti^{4+} ions, considering that the ionic radius of Ti^{4+} (0.605 Å) is larger than that of the Mn^{4+} (0.530 Å). The refined parameters are presented in Table I for various Ti doping. Ti^{4+} ions partially

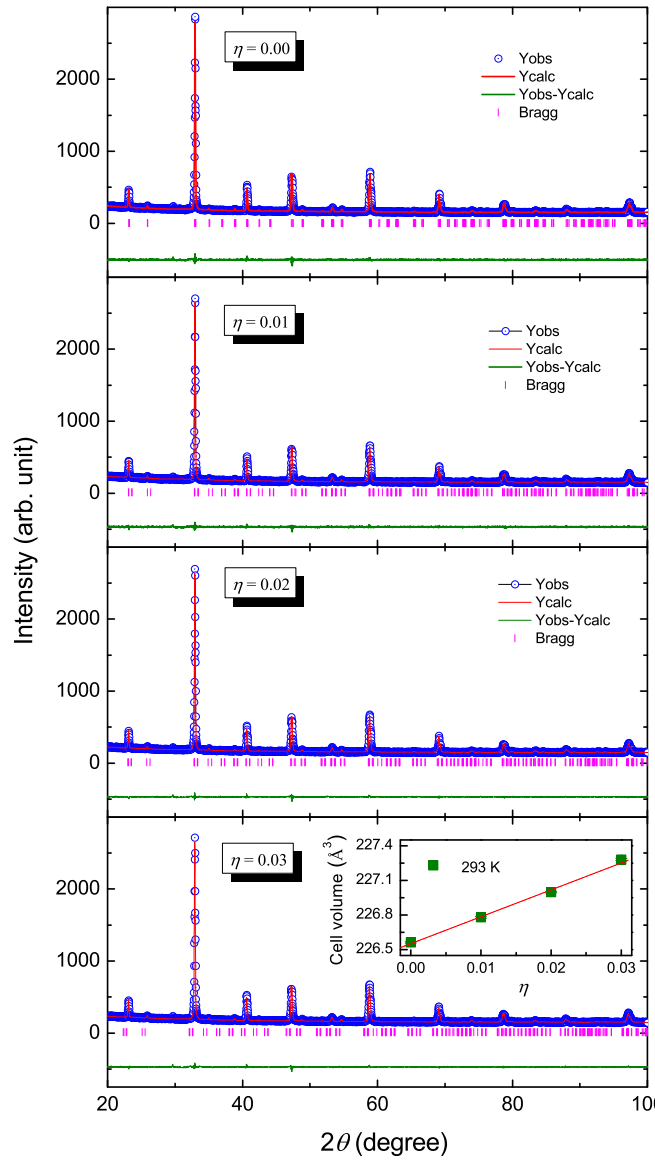

FIG. 1. X-ray diffraction pattern of $Sm_{0.55}Sr_{0.45}Mn_{1-\eta}Ti_{\eta}O_3$ ($0 \leqslant \eta \leqslant 0.03$) at room temperature. The bottom curves (Yobs-Ycalc) are due to the difference between the observed data, and the refinement data and the vertical bars indicate the Bragg peak positions for Cu $K\alpha_1$ and Cu $K\alpha_2$ radiations. The inset shows the Ti doping dependence of the unit-cell volume at room temperature.

TABLE I. Refined parameters for the $Sm_{0.55}Sr_{0.45}Mn_{1-\eta}Ti_{\eta}O_3$ ($0 \leqslant \eta \leqslant 0.03$) compound at room temperature with the *Pnma* space group. a, b, c are the lattice parameters, and v is the unit-cell volume. Numbers in parentheses are the statistical errors. U_{iso} is the isotropic atomic displacement parameter, and χ^2 is the goodness of fit.

Composition	$\eta = 0$	$\eta = 0.01$	$\eta = 0.02$	$\eta = 0.03$
a (Å)	5.43027(11)	5.43271(13)	5.43433(9)	5.43703(13)
b (Å)	7.66747(14)	7.66989(16)	7.67356(11)	7.67702(16)
c (Å)	5.44146(9)	5.44253(11)	5.44352(9)	5.44512(12)
v (Å^3)	226.563(7)	226.781(8)	226.999(6)	227.280(9)
χ^2 (%)	3.34	3.25	3.17	3.17
U_{iso} (Å^2), Sm(Sr)	0.0052(4)	0.0067(4)	0.0070(4)	0.0077(4)
U_{iso} (Å^2), Mn(Ti)	0.0021(6)	0.0049(6)	0.0032(5)	0.0048(6)
U_{iso} (Å^2), O1(O2)	−0.003(2)	0.007(2)	0.002(2)	0.0033(19)

and randomly substitute isovalent Mn^{4+} ions, and it is believed that like other Ti-doped manganites, the substitution of Ti in the present system also increases the average (Mn,Ti)-O bond lengths, and decreases the ⟨(Mn,Ti)-O-(Mn,Ti)⟩ bond angle and hence reduces the bandwidth of the system [30].

B. Magnetic and transport properties

Figure 2(a) shows the temperature dependence of magnetization of $Sm_{0.55}Sr_{0.45}Mn_{1-\eta}Ti_{\eta}O_3$ for $\eta = 0$, 0.01, 0.02, and 0.03. The parent compound SSMO shows a sharp FM-PM transition at $T_c \sim 128$ K, estimated as the temperature at which the temperature coefficient of magnetization (dM/dT) exhibits a deep minimum [inset of Fig. 2(b)]. However, the magnetization data are not the same in the warming and cooling cycles, but they exhibit a strong irreversibility of ∼4.5 K, demonstrating the first-order nature of the FM transition. With increasing η the ferromagnetism is suppressed, which is indicated through the reduction of magnetization as well as a strong decrease in T_c. T_c is observed to decrease approximately linearly with η at the rate of 22 K%$^{-1}$ [Fig. 2(b)], which is much higher than that observed in several other Ti-doped FM manganites [30–32]. In addition to T_c, the width of thermal hysteresis also changes drastically with Ti doping, which is shown in Fig. 2(b). Remarkably, only 3% Ti doping increases ΔT from 4.5 to 23.4 K. For all the samples with

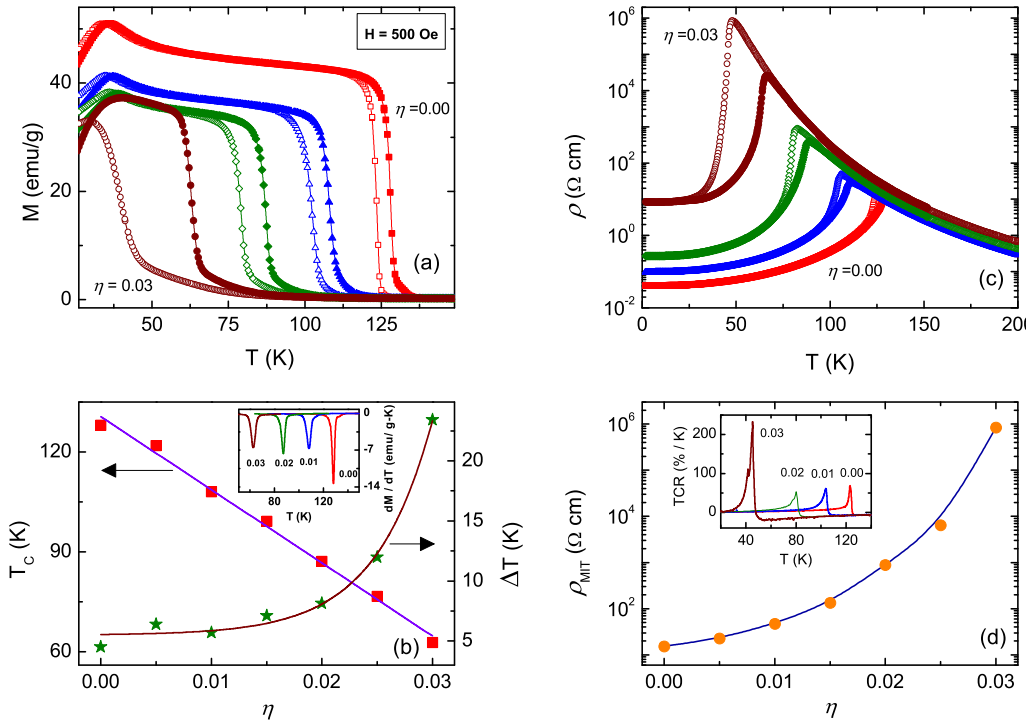

FIG. 2. (a) Temperature (T) dependence of magnetization (M) of $Sm_{0.55}Sr_{0.45}Mn_{1-\eta}Ti_{\eta}O_3$ for $\eta = 0.0$, 0.01, 0.02, and 0.03. Closed and open symbols represent heating and cooling cycles, respectively. (b) Ferromagnetic-paramagnetic transition temperature, T_c (in the warming cycle), and thermal hysteresis width (ΔT) as a function of Ti concentration (η). The inset shows the T dependence of dM/dT for different η. (c) Temperature profile of resistivity (ρ) for different η both in warming (closed symbol) and cooling (open symbol) cycles. (d) Peak resistivity at the metal-insulator transition (ρ_{MIT}) as a function of η. ρ_{MIT} is derived from the cooling cycle of the $\rho(T)$ curve. The inset shows the temperature coefficient of resistivity (TCR) as a function of T for different η.

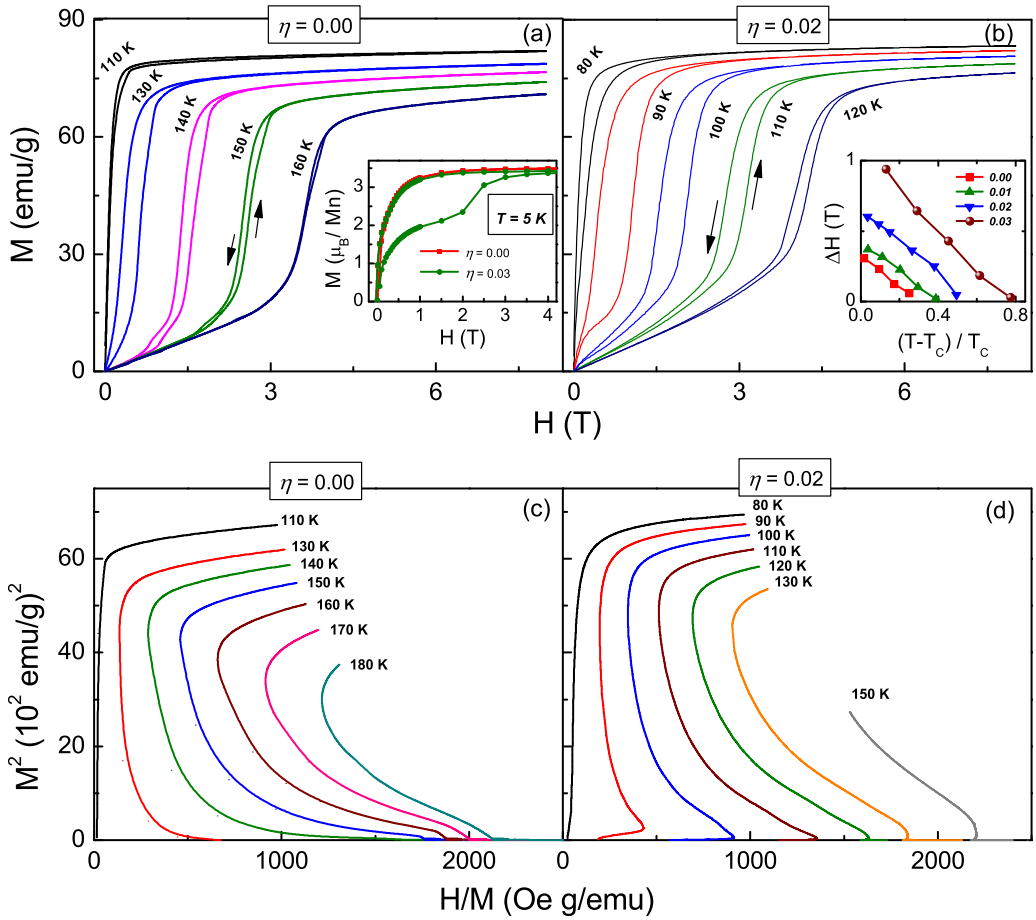

FIG. 3. $M(H)$ isotherms of $Sm_{0.55}Sr_{0.45}Mn_{1-\eta}Ti_{\eta}O_3$ for (a) $\eta = 0$ and (b) $\eta = 0.02$. The inset of (a) represents an $M(H)$ hysteresis loop measured at 5 K, while the inset of (b) shows the hysteresis width (ΔH) of $M(H)$ isotherms between increasing and decreasing fields as a function of reduced temperature, $(T - T_c)/T_c$. Arrott plots (M^2 vs H/M) for (c) $\eta = 0$ and (d) 0.02.

$0 \leqslant \eta \leqslant 0.03$, we observe that a cusp appears in the $M(T)$ curve at around 35 K, and M decreases slowly below the cusp. This phenomenon is due to the ordering of the Sm sublattice. In the low-temperature regime, the decrease of M with decreasing T may be related to the formation of magnetic domains, magnetic inhomogeneities, etc. [15,16,37]. It may be mentioned that M has also been measured for a sample with a slightly higher Ti concentration ($\eta = 0.04$), but no FM transition has been observed down to 2 K. In the resistivity curve [Fig. 2(c)], the MIT is observed at $T_{MI} \approx 129$ K ($\eta = 0$), corresponding to the resistivity maximum. The presence of thermal hysteresis in the $\rho(T)$ curve around T_{MI} indicates the first-order nature of the transition. Similar to magnetization, as Ti substitution proceeds, T_{MI} decreases linearly while the width of the thermal hysteresis in $\rho(T)$ increases almost exponentially. Depending on the degree of influence of B-site doping on charge conduction, the whole temperature region in the $\rho(T)$ curve can be divided into three main parts. At low temperatures well below T_{MI}, ρ increases sharply with increasing Ti content. As η increases from 0 to 0.03, the residual resistivity increases almost by a factor 10^4. The value of residual resistivity ($\sim$8.5 Ω cm) for $\eta = 0.03$ is well above the Ioffe-Regel limit ($\sim 10^{-3}$ Ω cm) to observe metallic behavior, suggesting that the ground state is not a homogeneous ferromagnet, rather it can be a coexistence of FM and short-range CO states. Similar to residual resistivity, the peak resistivity at the MIT (ρ_{MIT}) is also enhanced by a factor as high as 10^5 with increasing η from 0 to 0.03, as shown in Fig. 2(d). In the PM insulating state well above T_{MI}, the effect of Ti substitution on ρ is relatively weaker as compared to that in the low-temperature region. For all the studied samples, the temperature coefficient of resistivity [TCR $= \frac{1}{\rho}(\frac{d\rho}{dT})$] exhibits a very sharp peak at T_c [inset of Fig. 2(d)], expected for a first-order phase transition. From the figure, one can see that the maximum value of TCR is almost the same for $0 \leqslant \eta \leqslant 0.02$, but it increases abruptly for $\eta = 0.03$. As the MIT for $\eta = 0.03$ is much sharper as compared to other compositions, TCR is very large for this composition in spite of the large value of ρ. This behavior is quite unexpected. Normally, disordering in the active Mn-O-Mn network is supposed to broaden the FM transition. The inset of Fig. 3(a) shows a magnetization hysteresis loop at 5 K for $\eta = 0$ and 0.03. We have measured $M(H)$ at 5 K for $\eta = 0, 0.01, 0.02$, and 0.03, but for clarity only $\eta = 0$ and 0.03 data are presented in the figure. As in the case of a typical soft ferromagnet, the magnetization for the samples with $\eta \leqslant 0.02$ increases rapidly with the application of a field and tends to saturate at a relatively low-field strength. However, for $\eta = 0.03$, the nature of the $M(H)$ curve at 5 K is not like a simple ferromagnet, but it exhibits a metamagnetic transition along with field hysteresis. Ti substitution weakens the FM

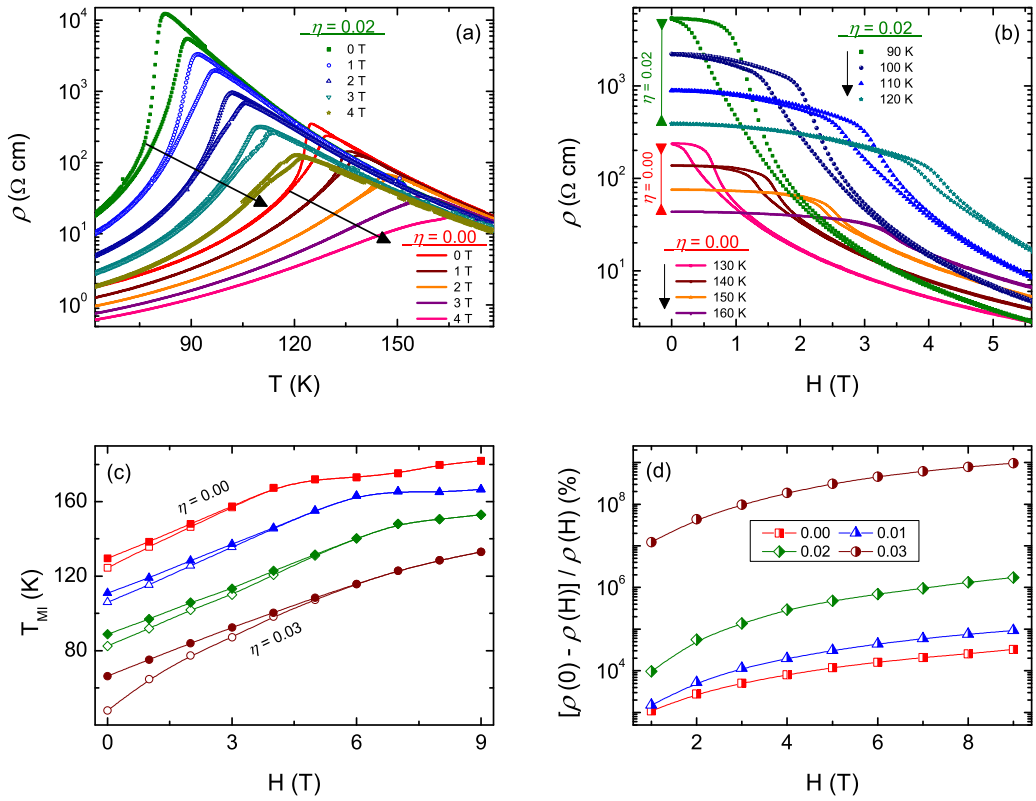

FIG. 4. (a) ρ vs T curves at different H (=0, 1, 2, 3, and 4 T) for $\eta = 0$ (lines) and 0.02 (symbols). Data recorded during warming and cooling cycles are shown in the figure. The arrow indicates the direction of increasing field. (b) H dependence of ρ at different temperatures for $\eta = 0$ (lines) and 0.02 (symbols). (c) The variation of metal-insulator transition temperature ($T_{\rm MI}$) with H for different η. Closed and open symbols are the $T_{\rm MI}$'s derived from the heating and cooling cycles of $\rho(T)$ curves, respectively. (d) Magnetoresistance $\{[\rho(0) - \rho(H)]/\rho(H)\}$ as a function of H for different η. It is calculated at $T = T_{\rm MI}(H = 0)$.

ordering in the parent compound and may favor the formation of a short-range CO state. The saturation magnetization for different η is determined by extrapolating the high-field part of the $M(H)$ curves to $H = 0$. The estimated values of saturation magnetization are $3.51\mu_B$, $3.46\mu_B$, $3.45\mu_B$, and $3.44\mu_B$ per Mn atom for $\eta = 0$, 0.01, 0.02, and 0.03, respectively. These values are slightly lower than their respective theoretical values of $3.55\mu_B$, $3.52\mu_B$, $3.49\mu_B$, and $3.46\mu_B$ per Mn atom, suggesting that the decrease of magnetization with Ti doping is not only due to the dilution of the Mn^{4+} atom but also due to the weakening of exchange coupling. In the vicinity of T_c, $M(H)$ isotherms for $\eta = 0$ and 0.02 are presented in Figs. 3(a) and 3(b), respectively. $M(H)$ curves below T_c are typical of a ferromagnet with small hysteresis between an increasing and decreasing field. Initially, M increases rapidly with H and then tends to saturate, and the saturation value of M gradually decreases with increasing temperature. Above T_c, we observe an S-shaped $M(H)$ isotherm, which indicates a metamagnetic phase transition. With increasing H, first M increases almost linearly and then suffers a steplike jump, indicative of reentrant ferromagnetism. Such a steplike jump in M along with the hysteresis are a manifestation of a field-induced first-order PM-FM phase transition. The inset of Fig. 3(b) shows the temperature [reduced temperature, $(T - T_c)/T_c$] dependence of the width of the field hysteresis (ΔH) in $M(H)$ isotherms for different η. For $\eta = 0$, ΔH just above T_c (~128 K) is ~0.3 T, which decreases almost linearly with increasing T and eventually vanishes at a temperature that is around $1.3T_c$. ΔH is observed to increase with increasing η but decreases almost at the same rate as that for $\eta = 0$ with increasing T. Figures 3(c) and 3(d) show the Arrott plots (M^2 versus H/M), which offers a criterion for determining whether the FM to PM phase transition is first-order or second-order purely by the magnetic method [38]. According to Banerjee criterion, if the slope of the Arrott plot is positive, then the FM transition is second-order in nature, and for a first-order transition the slope is negative [39]. The undoped compound shows a negative slope in M^2 versus H/M plot, and this behavior persists for $\eta \leqslant 0.03$, which means that the FM transition in all samples is first-order.

We now investigate the effect of an external magnetic field on the FM phase transition in $Sm_{0.55}Sr_{0.45}Mn_{1-\eta}Ti_\eta O_3$ ($0 \leqslant \eta \leqslant 0.03$). The temperature and field dependences of ρ for different η (0 and 0.02) are shown in Figs. 4(a) and 4(b). Figure 4(a) shows that the effect of H on ρ is maximum in the vicinity of $T_{\rm MI}$, whereas ρ remains almost unchanged well above $T_{\rm MI}$. For all samples, the peak resistivity and resistivity below $T_{\rm MI}$ are observed to reduce strongly with the field. Well below $T_{\rm MI}$, the application of a magnetic field enhances the spin-polarized tunneling through grain boundaries, and as a result residual resistivity decreases rapidly with the field. As shown in Fig. 4(b), resistivity evolves with

H in an opposite way to that of magnetization [Figs. 3(a) and 3(b)]. Just above T_c, ρ drops sharply with H along with field hysteresis, a consequence of the first-order phase transition. With increasing temperature, the sharpness of the field-induced change in ρ diminishes, and the width of the field hysteresis gradually becomes narrow and finally vanishes above a critical temperature, T_{cr}. The resultant T_{MI}-H phase diagram for various Ti concentrations is plotted in Fig. 4(c). As H increases, the width of thermal hysteresis in ρ gradually decreases and the two phase-transition lines, corresponding to the warming and cooling processes, merge with one another at a critical magnetic field (H_{cr}). This feature indicates that an external field suppresses the first-order nature of the transition, the transition becomes a crossover above H_{cr}, and the value of the critical field H_{cr} increases from 4 to 6 T as η increases from 0 to 0.03. In the regime of $H < H_{cr}$, T_{MI} for all samples increases linearly with H at an average rate of 9 K/T but at a slower rate above H_{cr}. We have also calculated magnetoresistance (MR) at $T = T_{MI}$ ($H = 0$) for $0 \leqslant \eta \leqslant 0.03$. Here, MR is defined as $\mathrm{MR} = \Delta\rho/\rho(H) = [\rho(0) - \rho(H)]/\rho(H) \times 100\%$, where $\rho(0)$ and $\rho(H)$ are the values of resistivity at zero field and at an applied field H, respectively. Figure 4(d) shows the typical magnetic-field dependence of MR for different η. For $\eta = 0$, the value of MR at $H = 1$ T is $1.1\times10^4\%$, which increases with H and becomes $3.2\times10^4\%$ for $H = 9$ T. MR enhances with Ti doping, and the most fascinating effect is observed for the composition $\eta = 0.03$, where MR reaches $1.2\times10^7\%$ for $H = 1$ T only and it becomes $\sim10^9\%$ for $H = 9$ T. The observed value of MR is much higher as compared with several other FM manganites.

As mentioned earlier, there are very few reports on the effect of Mn-site doping on the physical properties of narrowband manganites exhibiting a first-order FM to PM phase transition, and those studies are mainly concentrated on the doping dependence of T_c and magnetotransport properties close to the transition point [28]. However, doping at the Mn site in narrowband FM manganites close to the multicritical point is expected to reveal a more interesting scenario. In the present work, we have shown that Ti doping at the Mn site in $Sm_{0.55}Sr_{0.45}MnO_3$ decreases T_c and only 4% Ti doping completely destroys the ferromagnetism and metallic behavior. Both the thermal hysteresis and the sharpness of the resistive transition associated with the first-order FM-PM transition are observed to increase dramatically with Ti content. In contrast to narrowband manganites, the FM transition in wide-band manganites is usually second-order, and the effect of impurity on the physical properties is much weaker. As a result, the physical parameters such as T_c, ρ, $\Delta\rho/\rho(H)$, etc., change at a much slower rate with impurity concentration. For example, the resistive transition at the FM-PM transition in wide-band manganites is not very sensitive to impurity concentration. On the other hand, in $Sm_{0.55}Sr_{0.45}Mn_{1-\eta}Ti_\eta O_3$, the lattice distortion at the impurity site causes an abrupt increase in resistivity at the MIT and hence the resistive transition becomes extremely sharp with Ti doping. The large value of TCR as compared with several manganite thin films and bulk samples [40–43] and huge MR under the application of a 1 T magnetic field only may have technological applications. In addition to this rich variety of exotic phenomena, we have presented a simple model Hamiltonian calculation, to be discussed in the next section, which qualitatively explains the experimental results.

C. Theoretical simulation

We consider a two-band model Hamiltonian in two dimensions for manganites in the large Hund's coupling limit ($J_H \to \infty$) [2,44] to study the role of Ti doping on transport and magnetic properties of SSMO:

$$\mathcal{H} = -\sum_{\langle ij\rangle\sigma}^{\alpha\beta} t_{\alpha\beta}^{ij} d_{i\alpha\sigma}^{\dagger} d_{j\beta\sigma} + J\sum_{\langle ij\rangle} \mathbf{S}_i \cdot \mathbf{S}_j - \lambda \sum_i \mathbf{Q}_i \cdot \boldsymbol{\tau}_i + \frac{K}{2}\sum_i \mathbf{Q}_i^2 + \sum_i \epsilon_i n_i,$$

where e_g electrons hop between nearest-neighbor sites i and j with amplitude $t_{\alpha\beta}^{ij}$ (for two orbitals a and b). The hopping amplitudes $t_{\alpha\beta}^{ij}$ depend upon the orientation of Mn t_{2g} spins at the sites i and j. For details, please see Ref. [2]. J and λ denote the antiferromagnetic superexchange interaction between Mn t_{2g} spins ($\mathbf{S}_i$) and the electron-phonon interaction between the e_g electrons and the Jahn-Teller phonons $\mathbf{Q}_i$ in the adiabatic limit, respectively. We treat all $\mathbf{S}_i$ (with $|\mathbf{S}_i| = 1$) and $\mathbf{Q}_i$ (with stiffness of the Jahn-Teller modes $K = 1$) as classical [45,46], and we measure all parameters (J, λ, and temperature T) in the units of hopping amplitude t_{aa}.

This minimal model Hamiltonian $\mathcal{H}$ reproduces the correct sequence of magnetic phases [35,47,48]. Typical $\lambda \sim 1.6$–1.7 values with $J = 0.1$ reproduce the colossal magnetoresistive properties of intermediate bandwidth manganites qualitatively [48]. For $\lambda = 1.65$ and $J = 0.1$, a CE-type insulating phase can be reproduced for electron density $n = 0.5$, whereas the FM window spans the range $0.6 < n < 0.7$ similar to intermediate bandwidth manganites. Here, we will concentrate our calculations for $n = 0.65$ at which FM T_c is maximum. Recall that in the (Sm,Sr) manganite system, T_c is optimum for $n = 0.55$ [16] and our experiments are carried out at that electron density. The effect of A-site disorder (due to the mismatch between the ionic radii of Sm^{3+} and Sr^{2+}) is taken into account by adding $\sum_i \epsilon_i n_i$ in the Hamiltonian, where ϵ_i is the quenched binary disorder potential with values $\pm\Delta$. We use $\Delta = 0.1$ and also checked our calculations for $\Delta = 0$ and 0.2 to show that strong quenched disorder suppresses T_c more rapidly with Ti doping.

Next, in order to incorporate the effect of nonmagnetic B-site dopants (Ti^{4+} in the present case), we modify the Hamiltonian as shown schematically in the inset of Fig. 5(a). A large energy level V (= 5) is used at Ti sites by adding $V\sum_i n_i$ to the Hamiltonian [44]. For $V = 5$, the electron density at the impurity site is close to zero. The electron-phonon coupling is irrelevant at Ti sites, and for this reason we use λ at impurity sites $\lambda_{Ti} = 0$. Superexchange interaction (J') between the impurity site and the nearest Mn sites is modified to zero from 0.1 [inset of Fig. 5(a)]. Although our Hamiltonian has a spin moment at each impurity site, that moment is very weakly connected to the rest of the system due to $J' = 0$ and the large on-site potential V (=5). So, these moments at impurity sites do not affect the magnetism and are not taken into account while calculating the ferromagnetic order. From our experimental results, it is clear that with Ti doping, the unit-cell volume

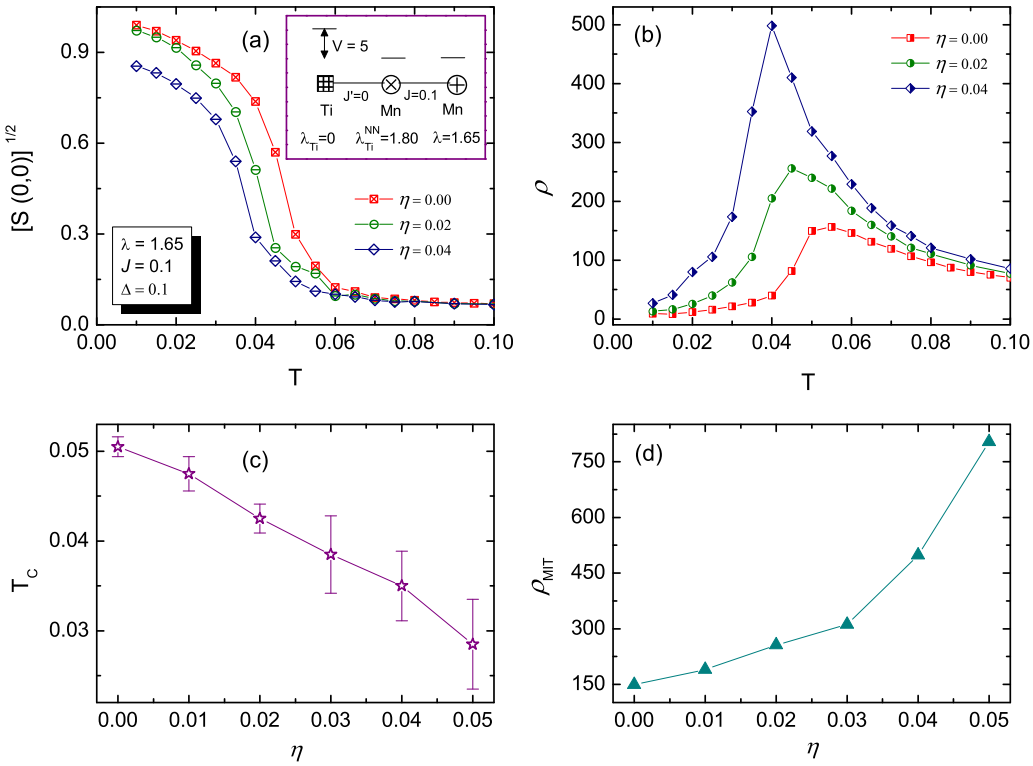

FIG. 5. Temperature dependence of (a) the square-root of ferromagnetic structure factor $S(0,0)$ (magnetization) and (b) resistivity (ρ) for dopant concentration $\eta = 0$, 0.02, and 0.04. (c) Ferromagnetic transition temperature, T_c, with various dopant concentrations η. (d) Peak resistivity at the metal-insulator transition (ρ_{MIT}) as a function of η. The schematic figure in the inset of (a) shows the relevant levels on Ti and Mn sites, and the coupling between these atoms. For notations, please see the text.

of the system increases (inset of Fig. 1), and as a result the bandwidth of the system decreases [30]. To take this effect into account, we modify the λ values at the Mn sites ($\lambda_{Ti}^{NN} = 1.80$) that are nearest neighbor to Ti ions. Recall that λ is measured in units of kinetic energy, and thus larger λ corresponds to a smaller bandwidth. Large λ_{Ti}^{NN} helps in localizing the electrons at those sites, and as a result Mn^{3+} look-alike ions surround the Ti^{4+} ions that minimize the Coulomb repulsion.

We use an exact diagonalization scheme for the itinerant electron system for each configuration of the background classical variables $\mathbf{S}_i$ and $\mathbf{Q}_i$. We use a Monte Carlo sampling technique based on the traveling cluster approximation [48,49] to access large system sizes. All physical quantities, such as the ferromagnetic structure factor and the resistivity, are thermally averaged over ten different samples (starting from ten different initial realizations of the quenched disorder and classical variables).

The temperature dependence of the square root of the ferromagnetic structure factor $S(0,0)$, which is equivalent to M, and the resistivity ρ with Ti concentration η are shown

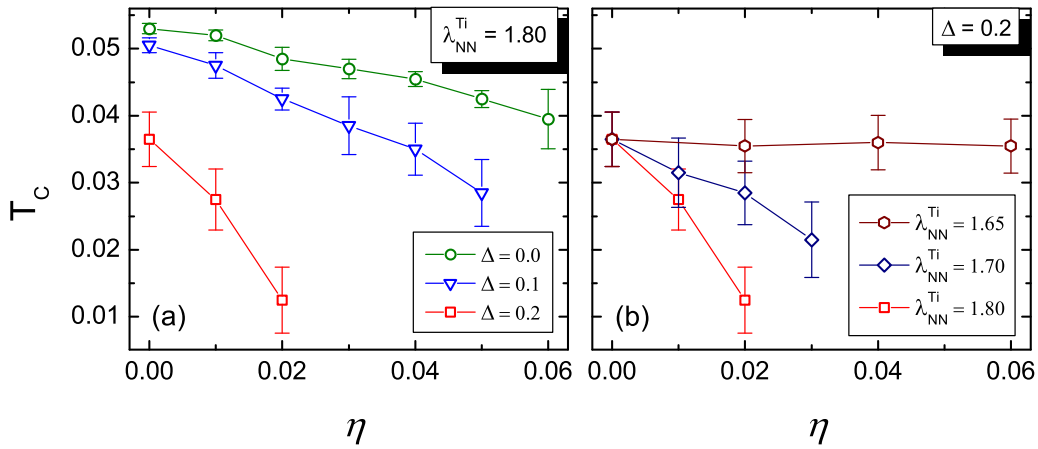

FIG. 6. Variation of T_c with η for $\lambda = 1.65$ and $J = 0.1$: (a) different Δ values (using $\lambda_{Ti}^{NN} = 1.80$) and (b) different λ_{Ti}^{NN} values (using $\Delta = 0.2$).

in Figs. 5(a) and 5(b), respectively. $S(0,0)$ is obtained by calculating $S(\mathbf{q}) = \frac{1}{N^2(1-\eta)^2}\sum_{ij}\mathbf{S}_i \cdot \mathbf{S}_j e^{i\mathbf{q}\cdot(\mathbf{r}_i-\mathbf{r}_j)}$ at wave vector $\mathbf{q} = (0,0)$ for Mn sites. The resistivity, in units of $\hbar a/\pi e^2$ (a denotes a lattice constant), is obtained from the dc limit of the conductivity (calculated using the Kubo-Greenwood formalism) [50,51]. T_c decreases approximately linearly, and the resistivity peak increases very fast with η, as shown in Figs. 5(c) and 5(d), respectively, and it agrees qualitatively with our experiments.

For $\Delta = 0.2$ ($\Delta = 0$) and $\lambda_{\mathrm{Ti}}^{\mathrm{NN}} = 1.80$, T_c decreases faster (slower) than that for $\Delta = 0.1$ as shown in Fig. 6(a). This shows that disorder also plays an important role in suppressing T_c. We also use $\lambda_{\mathrm{Ti}}^{\mathrm{NN}} = 1.70$ for the $\Delta = 0.2$ case and find that T_c decreases linearly, albeit up to $\eta = 0.03$, as shown in Fig. 6(b). However, for $\lambda_{\mathrm{Ti}}^{\mathrm{NN}} = 1.65$ (i.e., without modifying λ at nearest-neighbor Mn ions of the Ti site), T_c remains more or less the same until $\eta = 0.06$ for $\Delta = 0.2$. So, we believe that lattice distortions around the Ti ions increase, and they localize the electrons. As a result, T_c decreases with Ti doping.

IV. CONCLUSION

The effect of Ti doping on the magnetotransport properties of $Sm_{0.55}Sr_{0.45}Mn_{1-\eta}Ti_\eta O_3$ ($0 \leqslant \eta \leqslant 0.03$) has been studied. All these samples undergo a first-order FM metal to PM-insulator transition at T_c (or T_{MI}) along with hysteresis. With increasing Ti concentration, T_c decreases linearly while the magnetoresistance increases very rapidly. Our theoretical calculations show that T_c decreases due to the increase of lattice distortion around the Ti ions. The application of external field H stabilizes the FM phase and thus weakens the first-order nature of the transition. The critical magnetic field where the first-order transition becomes a crossover increases with Ti doping.

[1] C. N. R. Rao and B. Raveau, *Colossal Magnetoresistance, Charge Ordering and Related Properties of Manganese Oxides* (World Scientific, Singapore, 1998).
[2] E. Dagotto, T. Hotta, and A. Moreo, Phys. Rep. **344**, 1 (2001).
[3] M. B. Salamon and M. Jaime, Rev. Mod. Phys. **73**, 583 (2001).
[4] E. Dagotto, Science **309**, 257 (2005).
[5] Y. Tokura, Rep. Prog. Phys. **69**, 797 (2006).
[6] P. K. Siwach, H. K. Singh, and O. N. Srivastava, J. Phys.: Condens. Matter **20**, 273201 (2008).
[7] H. Y. Hwang, S. W. Cheong, P. G. Radaelli, M. Marezio, and B. Batlogg, Phys. Rev. Lett. **75**, 914 (1995).
[8] Y. Tokura, H. Kuwahara, Y. Moritomo, Y. Tomioka, and A. Asamitsu, Phys. Rev. Lett. **76**, 3184 (1996).
[9] L. M. Rodriguez-Martinez and J. P. Attfield, Phys. Rev. B **54**, R15622(R) (1996); **58**, 2426 (1998); **63**, 024424 (2000).
[10] J. P. Attfield, Int. J. Inorg. Mater. **3**, 1147 (2001).
[11] Y. Tomioka, Y. Okimoto, J. H. Jung, R. Kumai, and Y. Tokura, Phys. Rev. B **68**, 094417 (2003).
[12] D. Akahoshi, M. Uchida, Y. Tomioka, T. Arima, Y. Matsui, and Y. Tokura, Phys. Rev. Lett. **90**, 177203 (2003).
[13] G. L. Liu, J. S. Zhou, and J. B. Goodenough, Phys. Rev. B **70**, 224421 (2004).
[14] Y. Tomioka and Y. Tokura, Phys. Rev. B **70**, 014432 (2004).
[15] L. M. Fisher, A. V. Kalinov, I. F. Voloshin, N. A. Babushkina, D. I. Khomskii, Y. Zhang, and T. T. M. Palstra, Phys. Rev. B **70**, 212411 (2004).
[16] Y. Tomioka, H. Hiraka, Y. Endoh, and Y. Tokura, Phys. Rev. B **74**, 104420 (2006).
[17] P. Sarkar, P. Mandal, A. K. Bera, S. M. Yusuf, L. S. Sharath Chandra, and V. Ganesan, Phys. Rev. B **78**, 012415 (2008).
[18] L. Demkó, I. Kézsmárki, G. Mihály, N. Takeshita, Y. Tomioka, and Y. Tokura, Phys. Rev. Lett. **101**, 037206 (2008).
[19] P. Sarkar, P. Mandal, K. Mydeen, A. K. Bera, S. M. Yusuf, S. Arumugam, C. Q. Jin, T. Ishida, and S. Noguchi, Phys. Rev. B **79**, 144431 (2009).
[20] P. Sarkar, S. Arumugam, P. Mandal, A. Murugeswari, R. Thiyagarajan, S. Esaki Muthu, D. Mohan Radheep, C. Ganguli, K. Matsubayshi, and Y. Uwatoko, Phys. Rev. Lett. **103**, 057205 (2009).
[21] N. Khan, P. Sarkar, A. Midya, P. Mandal, and P. K. Mohanty, Sci. Rep. **7**, 45004 (2017).
[22] Y. Moritomo, A. Machida, S. Mori, N. Yamamoto, and A. Nakamura, Phys. Rev. B **60**, 9220 (1999).
[23] T. Kimura, R. Kumai, Y. Okimoto, Y. Tomioka, and Y. Tokura, Phys. Rev. B **62**, 15021 (2000).
[24] A. Machida, Y. Moritomo, K. Ohoyama, T. Katsufuji, and A. Nakamura, Phys. Rev. B **65**, 064435 (2002).
[25] H. Sakai, K. Ito, R. Kumai, and Y. Tokura, Phys. Rev. B **76**, 155112 (2007).
[26] C. L. Lu, X. Chen, S. Dong, K. F. Wang, H. L. Cai, J.-M. Liu, D. Li, and Z. D. Zhang, Phys. Rev. B **79**, 245105 (2009).
[27] C. Lu, N. Hu, M. Yang, S. Xia, H. Wang, J. Wang, Z. Xia, and J. M. Liub, Sci. Rep. **4**, 4902 (2014).
[28] A. Maignan, F. Damay, A. Barnabe, C. Martin, M. Hervieu, and B. Raveau, Philos. Trans. R. Soc. London, Ser. A **356**, 1635 (1998), and references therein.
[29] C. Martin, A. Maignan, M. Hervieu, C. Autret, B. Raveau, and D. I. Khomskii, Phys. Rev. B **63**, 174402 (2001).
[30] M. S. Kim, J. B. Yang, Q. Cai, X. D. Zhou, W. J. James, W. B. Yelon, P. E. Parris, D. Buddhikot, and S. K. Malik, Phys. Rev. B **71**, 014433 (2005).
[31] D. N. H. Nam, L. V. Bau, N. V. Khiem, N. V. Dai, L. V. Hong, N. X. Phuc, R. S. Newrock, and P. Nordblad, Phys. Rev. B **73**, 184430 (2006).
[32] D. N. H. Nam, N. V. Dai, T. D. Thanh, L. T. C. Tuong, L. V. Hong, N. X. Phuc, H. S. Hong, and N. V. Khien, Phys. Rev. B **77**, 224420 (2008).
[33] M. M. Saber, M. Egilmez, A. I. Mansour, I. Fan, K. H. Chow, and J. Jung, Phys. Rev. B **82**, 172401 (2010).
[34] I. Dhiman, A. Das, A. K. Nigam, and R. K. Kremer, J. Magn. Magn. Mater. **334**, 21 (2013).
[35] K. Pradhan, A. Mukherjee, and P. Majumdar, Europhys. Lett. **84**, 37007 (2008).
[36] G. Murugesan, R. Nithya, and S. Kalainathan, Powder Diffr. **31**, 77 (2016).
[37] R. P. Borges, F. Ott, R. M. Thomas, V. Skumryev, J. M. D. Coey, J. I. Arnaudas, and L. Ranno, Phys. Rev. B **60**, 12847 (1999).

[38] A. Arrott and J. E. Noakes, Phys. Rev. Lett. **19**, 786 (1967).
[39] B. K. Banerjee, Phys. Lett. **12**, 16 (1964).
[40] A. Goyal, M. Rajeswari, R. Shreekala, S. E. Lofland, S. M. Bhagat, T. Boettcher, C. Kwon, R. Ramesh, and T. Venkatesan, Appl. Phys. Lett. **71**, 2535 (1997); R. Shreekala, M. Rajeswari, S. P. Pai, S. E. Lofland, V. Smolyaninova, K. Ghosh, S. B. Ogale, S. M. Bhagat, M. J. Downes, R. L. Greene, R. Ramesh, and T. Venkatesan, *ibid.* **74**, 2857 (1999).
[41] R. Bathe, K. P. Adhi, S. I. Patil, G. Marest, B. Hannoyer, and S. B. Ogale, Appl. Phys. Lett. **76**, 2104 (2000).
[42] Y. Sun, M. B. Salamon, and S. H. Chun, J. Appl. Phys. **92**, 3235 (2002).
[43] D. M. Radheep, P. Sarkar, S. Arumugam, R. Suryanarayanan, and P. Mandal, J. Magn. Magn. Mater. **365**, 51 (2014).
[44] K. Pradhan, A. Mukherjee, and P. Majumdar, Phys. Rev. Lett. **99**, 147206 (2007).
[45] S. Yunoki, J. Hu, A. L. Malvezzi, A. Moreo, N. Furukawa, and E. Dagotto, Phys. Rev. Lett. **80**, 845 (1998).
[46] E. Dagotto, S. Yunoki, A. L. Malvezzi, A. Moreo, J. Hu, S. Capponi, D. Poilblanc, and N. Furukawa, Phys. Rev. B **58**, 6414 (1998).
[47] S. Yunoki, T. Hotta, and E. Dagotto, Phys. Rev. Lett. **84**, 3714 (2000).
[48] K. Pradhan and S. Yunoki, Phys. Rev. B **96**, 214416 (2017).
[49] S. Kumar and P. Majumdar, Eur. Phys. J. B **50**, 571 (2006).
[50] G. D. Mahan, *Quantum Many Particle Physics* (Plenum, New York, 1990).
[51] S. Kumar and P. Majumdar, Europhys. Lett. **65**, 75 (2004).